

Fabrication of diffractive optical elements by programmable thermocapillary shaping of thin liquid films

Ran Eshel^{1,¥}, Valeri Frumkin^{1,¥,§}, Matan Nice¹, Omer Luria¹, Boris Ferdman^{2,3}, Nadav Opatovski², Khaled Gommed¹, Maxim Shusteff⁴, Yoav Shechtman^{2,3}, and Moran Bercovici^{1,2,3,*}

¹ Faculty of Mechanical Engineering, Technion - Israel Institute of Technology, Haifa, 3200003 Israel

² Department of Biomedical Engineering, Technion - Israel Institute of Technology, Haifa, 3200003 Israel

³ Russell Berrie Nanotechnology Institute, Technion - Israel Institute of Technology, Haifa, 3200003 Israel

⁴ Lawrence Livermore National Laboratory, 7000 East Ave, Livermore, CA 94550, USA

[§] Current affiliation: Department of Mathematics, Massachusetts Institute of Technology, Cambridge, MA, 02139, United States

*Corresponding author: M.B. (mberco@technion.ac.il)

¥ Equal contribution

ABSTRACT

Diffractive optical elements (DOEs) enable precise manipulation of wavefronts and are widely used in a variety of optical systems. However, their fabrication relies on lithography or high precision machining processes that are long, expensive, and infrastructure-heavy. We here present a one-step rapid fabrication method that leverages the thermocapillary effect to shape thin liquid films into useful DOEs with sub-nanometeric surface roughness. Our system consists of a projection system, which illuminates any desired pattern onto the bottom of a fluidic chamber patterned with heat-absorbing pads. The heat induces surface tension gradients in the polymer-air interface, resulting in the polymer film deformation. The polymer is then photocured to yield a solid device. We developed a theoretical model that provides the required projection pattern to achieve a desired topography. Based on this model, we demonstrate the fabrication of several DOEs, including phase masks for extended depth of field imaging, and for 3D localization microscopy. Fabrication is completed in less than five minutes and requires no post-processing.

INTRODUCTION

Diffractive optical elements (DOEs) are used to manipulate light by introducing non-uniform phase accumulation through a carefully designed geometry and/or by changing the refractive index of the optical element [1]. DOEs are extensively used in a variety of applications, such as high precision microscopy [2,3], optical manipulation of particles [4], holographic fabrication [5], optical machine learning systems [6], optical communication systems [7], efficiency enhancement of photovoltaic modules [8], and correction of aberrations in space telescopes [9].

Typically, DOEs are created using clean room fabrication techniques, such as direct writing, focused ion beam milling, grayscale lithography and interferometric exposure [10], or by precise multi-axis mechanical processes such as diamond machining or magnetorheological finishing (MRF) [11,12]. However, all of these processes require significant and expensive infrastructure and highly-skilled operators, which lowers accessibility and drives high component costs. Furthermore, existing techniques do not allow for rapid prototyping which is much desired for driving research and design innovation.

Additive manufacturing methods are a natural candidate when considering fabrication of general 3D structures, yet traditional 3D printing cannot meet the surface quality standards required for optical components. Recent advancements, particularly in two-photon lithography, are beginning to bridge this gap. For example, Kotz et al. demonstrated the use of nanocomposites for fabrication of smooth optical surfaces [13]. Orange-Kedem et al. showed that the limitation of printing resolution can be mitigated by immersing a 3D printed phase mask into a liquid with a similar index of refraction, allowing the fabrication of DOEs using standard printers, and a similar approach of near-index matching has been suggested previously [14]. However, since fabrication time is directly proportional to the volume being printed, practical considerations currently limit 3D printing to small component sizes.

An alternative method for implementation of DOEs is by controlling the spatial index of refraction of the material. For example, Berto et al. demonstrated the use of patterned electrodes as a method for localized heating of a thermo-optic material, thus modifying the local index of refraction [15]. However, each desired refractive index distribution requires a dedicated lithography process to produce the electrodes. Furthermore, while controlling the current through the electrodes allows the device to be modulated on and off, its operation requires a sustained power supply. Wang et al. demonstrated a reprogrammable optical device, which utilized short pulses of high-density laser in order to change the refractive index of a dielectric material [16]. This high-density laser writing can be erased and rewritten, but relies on expensive short pulse lasers, and is currently limited to small lateral dimensions.

Another fabrication approach, which is neither additive nor subtractive, is to deform an optically transparent liquid film into a specific topography. The main advantage of this approach is its reliance on liquid-fluid interfaces, which are naturally smooth. Brown et al. demonstrated the use of dielectrophoresis forces, produced by a set of interdigitated electrodes, to create and solidify periodic deformation on the interface of a thin layer of polymer, thus producing diffraction gratings [17,18]. Recently, Gabay et al. [19] extended this concept to allow greater control over the deformation topography using more complex electrode patterns. However, similar to the work by Berto et al., this approach requires pre-patterning of electrodes using lithography processes.

An alternative actuation mechanism for manipulation of liquid interfaces is the use of the thermocapillary effect. Numerous studies have considered the use of this approach for patterning thin polymer films [20]. In particular, Nejati et al. [21] leveraged the Benard-Marangoni instability to drive short-wavelength deformation in a polymer film, yet this approach is limited to periodic structures. McLeod and Troian demonstrated deformations of nanoscale films using temperature-controlled structural elements brought in close proximity to the film, but this required the mechanical fabrication of conducting metal structures for each desired deformation [22].

In this work, we present for the first time the use of projected light patterns as a mechanism for driving deformations of a thin liquid film via the thermocapillary effect. As illustrated in Figure 1, we use a standard programmable digital micromirror device (DMD) to project a desired illumination intensity map onto a substrate containing an array of light-absorbing metal pads. This provides unprecedented control over the spatial temperature distribution in the substrate, which is translated to surface tension gradients and subsequent surface deformations in the overlaying

liquid film. When using a curable polymer, the resulting topography can be solidified to create a DOE with high surface quality. The entire process is completed in under 5 minutes, and the same light-absorbing substrate can be used again to create a different topography using a new projected pattern. While this approach could, in principle, be used also to create configurable devices, we here focus on fixed DOEs, which have a high photon efficiency and are much simpler to integrate into optical systems.

We provide complete details of the experimental system, and characterize its resolution and dynamic range as a function of the illumination intensity and of the absorbing array geometry. Furthermore, we derive a theoretical model for an inverse problem that provides the required temperature map for achieving a desired topography. Using the inverse-problem approach, we first demonstrate the fabrication of a one-dimensional diffraction grating component and characterize its performance, showing good agreement with theory. We then demonstrate the fabrication of an axisymmetric phase mask for extended depth of focus (EDOF) and show its implementation in imaging over a greater focal depth without reducing the numerical aperture. Finally, we demonstrate the fabrication of a non-axisymmetric saddle-point phase mask [23], and experimentally demonstrate its use in encoding of depth information in the point spread function (PSF) of nanoparticles, allowing microscopic three-dimensional particle tracking [24]. This work provides a method for low-cost customized fabrication of DOEs for industrial applications and allows for rapid prototyping of new DOE-based ideas in research.

RESULTS

Principles of the method

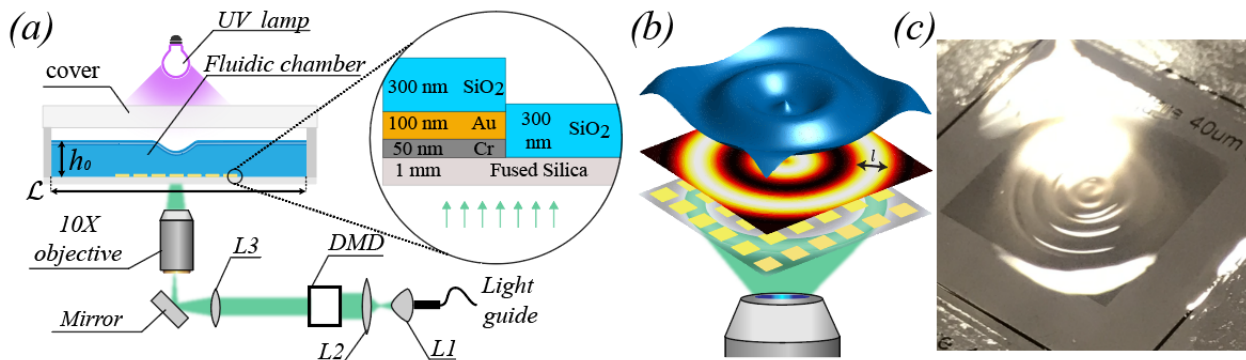


Figure 1 | Operational principle of the thermocapillary fluidic shaping method. (a) Schematic illustration of the experimental setup. The setup is based on a shallow fluidic chamber filled with a thin layer of a curable polymer. The bottom surface of the chamber is a glass substrate patterned with an array of metal pads designed to absorb light in the visible spectrum. A desired illumination pattern is projected onto the surface using a DMD-based system. The inset describes the internal structure of the metallic pads. (b) A desired illumination pattern is projected onto the metal pads, which absorb the light and create a corresponding temperature field. Heat is transferred from the pads, through the thin liquid layer and to the liquid-air interface, leading to surface tension gradients that drive the thermocapillary effect, resulting in spatial deformations of the free surface. (c) Image of the solidified polymer after exposure to UV illumination.

Figure 1 presents the principle of operation of the thermocapillary fluidic shaping method and the experimental setup used for its implementation. When localized heating is imposed on a gas-liquid interface, the liquid will flow outward along the free-surface from warmer regions with lower surface tension to colder regions with higher surface tension. This results in local deformation of the liquid film [25], and is known as the thermocapillary effect. The magnitude of the surface deformation is proportional to the local temperature gradients. We found that a convenient way to control these temperature gradients is to use light projection, whose spatial intensity can be easily programmed, to heat an array of absorbing metal pads patterned on the bottom of the fluidic chamber. The system uses a standard $< 3\text{W}$ microscope LED source and a standard DMD. The resulting increase in temperature is on the order of few degrees or less, and is sufficient to drive significant deformations.

The spatial resolution of the thermal patterning depends on the material properties of the substrate, the resolution of the projected pattern, and the geometry of the light absorbing metallic pad array. The composition of the metal pads was designed to maximize light absorbance across the UV-Vis spectrum of the light source, as shown in Figure 1c. Section 2 in the Supplementary Information provides characterization of the deformation magnitude and resolution in our system as a function of the illumination intensity and pad array density. As expected, the magnitude of the resulting deformation is proportional to both the illumination intensity and the area fraction occupied by the pads. The precise deformation magnitude and resolution depend on the specific heating pattern, with some tradeoff between the two (see theory section). However, typical values are on the order of $3\ \mu\text{m}$ maximum deformation and $5\ \mu\text{m}/\text{mm}$ spatial resolution.

The inverse problem — theory and implementation

Consider an open microfluidic chamber of length \mathcal{L} , containing a thin liquid film of thickness h_0 , as depicted in Figure 1(a). The chamber is heated from below by a light pattern that is absorbed by the metal pads array, resulting in temperature variations over a characteristic length l , $h_0 \ll l \ll \mathcal{L}$. For small variations in temperature, we can assume that the surface tension, σ , changes linearly with temperature, θ , according to

$$\sigma = \sigma_r - \beta(\theta - \theta_r), \quad (1)$$

where $\beta \equiv \frac{\partial\sigma}{\partial\theta}$ is defined as the thermocapillary coefficient and is assumed to be constant, θ_r is a reference temperature, and σ_r is the surface tension at that temperature. We assume that variations in temperature are sufficiently small such that changes in density and viscosity are negligible.

In Supplementary Information section 3 we provide a complete derivation of the governing equations. Briefly, we consider the continuity equation, the steady-state incompressible Navier-Stokes equations, and the steady-state advection-conduction heat equation. At the bottom of the film ($z = 0$) we require no-slip and no-penetration conditions on the flow, and set a fixed temperature distribution, θ_b . At the liquid air interface ($z = h(x, y)$) we impose the kinematic condition relating flow velocities to the shape of the deformed interface, a stress balance relating the stress tensor in the liquid to surface tension, and heat loss through Newton's cooling law. Using these equations and boundary conditions, we derive the dimensionless steady-state equation of the deformed liquid film driven by a non-uniform temperature distribution,

$$\vec{\nabla}_2 \cdot \left[\frac{S}{3} H^3 \vec{\nabla}_2 \nabla_2^2 H - \frac{G}{3} H^3 \vec{\nabla}_2 H - \frac{1}{2} H^2 \vec{\nabla}_2 \left(\frac{\vartheta_b + \Theta}{1 + BH} \right) \right] = 0. \quad (2)$$

Here $[X, Y, Z, H] = \left[\frac{x}{l}, \frac{y}{l}, \frac{z}{h_0}, \frac{h}{h_0} \right]$ are the dimensionless coordinates and film thickness scaled by the characteristic lateral and vertical dimensions, and $\vec{\nabla}_2 = \left(\frac{\partial}{\partial X}, \frac{\partial}{\partial Y} \right)$ and $\nabla_2^2 = \left(\frac{\partial^2}{\partial X^2} + \frac{\partial^2}{\partial Y^2} \right)$ are the two-dimensional gradient and Laplacian operators. We scale the velocity as $[U, V, W] = \frac{1}{U_0} [u, v, \frac{1}{\varepsilon} w]$, where $U_0 = \varepsilon \Delta\sigma / \mu$ is the characteristic velocity as derived from the tangential stress balance, with $\Delta\sigma = \beta \Delta\theta$ being the characteristic variation in surface tension, and $\Delta\theta = \theta_{b_{max}} - \theta_{b_{min}}$ the difference between the maximum and minimum temperature at that surface. μ is the dynamic viscosity of the liquid, and $\varepsilon = \frac{h_0}{l} \ll 1$ is the ratio of film thickness to characteristic lateral scale. We scale the temperature as $\vartheta = \frac{\theta - \bar{\theta}_b}{\Delta\theta}$ where $\bar{\theta}_b$ is the average temperature of the bottom surface. $S = \varepsilon^3 \frac{\sigma_r}{\mu U_0} = \varepsilon^2 \frac{\sigma_r}{\Delta\sigma}$ is the surface tension number, $B = \frac{\hbar h_0}{k}$ is the Biot number, \hbar is the heat transfer coefficient at the liquid-air interface, k is the thermal conductivity, $\Theta = \frac{\bar{\theta}_b - \theta_\infty}{\Delta\theta}$ is a ratio of temperature differences where θ_∞ is the ambient temperature, and $G = \varepsilon \frac{\rho h_0^2}{\mu U_0} g = \frac{\rho h_0^2}{\Delta\sigma} g$ is the dimensionless gravity.

Subjected to appropriate boundary conditions on the thickness of the liquid film (e.g. far from the heating region, the film thickness can be assumed to be known and uniform), equation 2 can be solved numerically to obtain a solution to the direct problem - the spatial deformation resulting from any prescribed temperature distribution $\vartheta_b(x, y)$. However, for engineering purposes, the inverse problem —seeking the temperature map that would yield a desired deformation— is of greater value. As shown in Supplementary Information section 3, for sufficiently small Gaussian curvatures, and assuming that far from the heating region the liquid film is flat, the temperature distribution can be obtained explicitly as a function of the desired deformation, $H(x, y)$,

$$\vartheta_b = \frac{(1 + BH)}{3} \left[2SH \nabla^2 H - S(\vec{\nabla}H)^2 - G(H^2 - 1) \right] - \Theta. \quad (3)$$

Figure 2 presents the use of the inverse problem for fabricating a desired topography. Figure 2a presents the prescribed topography composed of a set of concentric rings, with a maximum deformation relative to the baseline film thickness of $d_{desired} = 1.5 \mu m$. This topography is used as input into equation (3), with the constant parameters as defined in SI section 3, resulting in a temperature distribution $\vartheta_b(x, y)$. Since we do not have a direct relation between desired temperature and the required illumination intensity, we assume a linear dependence and perform a calibration measurement in which the illumination intensity map is set to $I(x, y) = I_0 \vartheta_b(x, y) / \max\{\vartheta_b(x, y)\}$, where I_0 is the maximum intensity of the light source. The resulting intensity map is presented in Figure 2b, and an image of the actual projected intensity map is presented in Figure 2c. We measure the resulting maximum deformation, d_{max} (which for this pattern was 2.2 μm), and repeat the projection using an intensity map that is scaled by $d_{desired}/d_{max}$ (i.e. 1.5/2.2). Figure 2d presents the resulting topography of the (solidified) deformed liquid film.

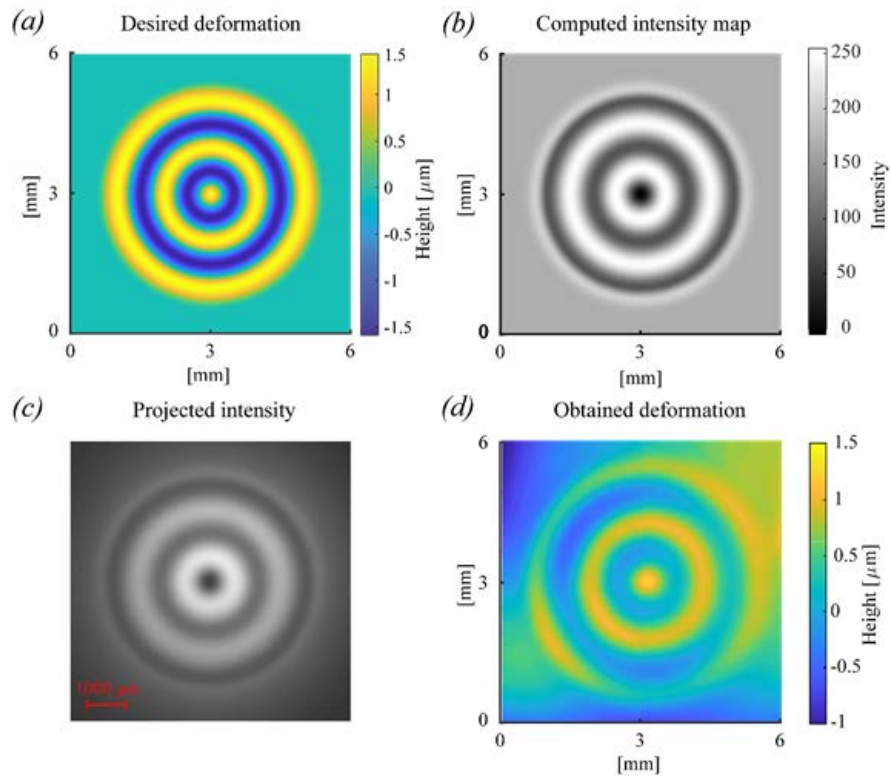


Figure 2 | Demonstration of a complete workflow for an inverse problem solution. (a) The desired topography defined in terms of the variation from a reference height. (b) The intensity map required in order to produce the desired deformation, as obtained from solving the inverse problem. (c) Image of the illumination pattern as obtained on the bottom surface of the fluidic device. (d) The resulting topography after curing the polymer as measured by the Digital holographic microscope (DHM) [26].

Applications

Figures 3-5 present several practical diffractive elements produced using the thermocapillary fluidic shaping approach.

Diffraction gratings are optical elements with a periodic structure, that diffract the incident light into several beams traveling in different directions, depending on the wavelength and the spatial periodic structure defining the angular spread. They are commonly used in monochromators for spectroscopic instruments [27].

Figure 3 presents a linear diffraction grating with a peak-to-peak periodicity of $400\ \mu\text{m}$ produced by projection of a sinusoidal illumination pattern. Figure 3a presents the projected pattern side-by-side with the resulting deformation, and Figure 3b presents the magnitude of the deformation along the centerline. We test the resulting element by measuring the diffractive angle for several wavelengths produced by monochromatic LEDs. Since the LEDs have a spectral bandwidth of approximately $50\ \text{nm}$, we use a weighted average of their spectrum (as provided by the

manufacturer) to define a representative wavelength for the analysis. As shown in Figure 3c, the results are in excellent agreement with the expected angle set by the element's periodicity. Figure 3d also presents a visual demonstration of white light diffracted through the grating and directly imaged by a camera sensor, clearly showing the separation of bands.

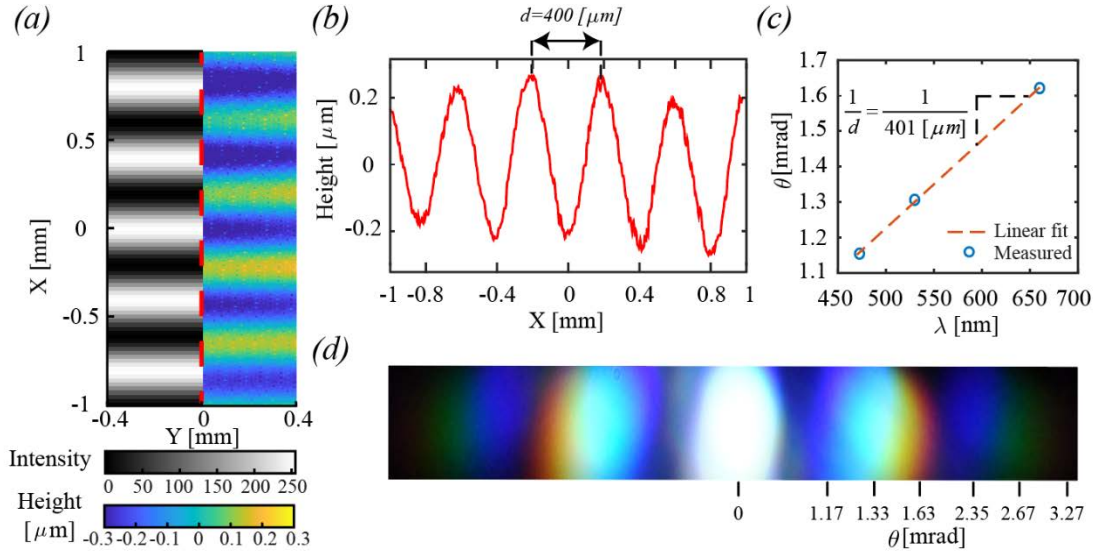


Figure 3 | Fabrication and testing of a linear diffraction grating. (a) Side-by-side image showing the projected light pattern (left) and the measured resulting topography (right). Regions with a higher projected intensity, and therefore a higher temperature, correspond to valleys in the topography. (b) The deformation magnitude along the center of the element, showing the spatial frequency ($400 \mu\text{m}$) and the resulting amplitude ($0.4 \mu\text{m}$) of the grating. (c) The measured diffractive angle for three wavelengths passing through the grating. The reciprocal of the slope of a least-square line matches well the designed grating spatial frequency. (d) Image of white light diffraction. The numbers along the scale indicate the center of each band along a horizontal centerline.

The depth of field of any optical system can be extended by reducing its numerical aperture, yet at the cost of reducing the amount of light collected. A number of studies have shown the ability to overcome this limitation and extend the depth of field without loss of photons, by positioning an appropriate phase mask in the systems' aperture [28,29]. Figure 4 presents the fabrication and testing of an extended depth of field (EDOF) phase mask designed by formulating a phase retrieval task as described by Nehme *et al.* [30]. The desired mask mold is translated into a light pattern (Figure 4b) using the inverse problem solution, and the thermocapillary fluidic shaping method is used to create a solid mold. We then cast PDMS onto the mold to create the phase mask itself, shown in Figure 4c. We position the mask in the Fourier plane of a $4f$ system and use it to image three targets positioned at different distances from the camera. As illustrated in Figure 4d, to ensure that the presence of the mask itself does not reduce the numerical aperture, we use a smaller fixed aperture in close proximity to the mask, acting as the aperture stop of the system. Figures 4e-f clearly show the additional depth of field gained by using the mask, yet with some loss of contrast.

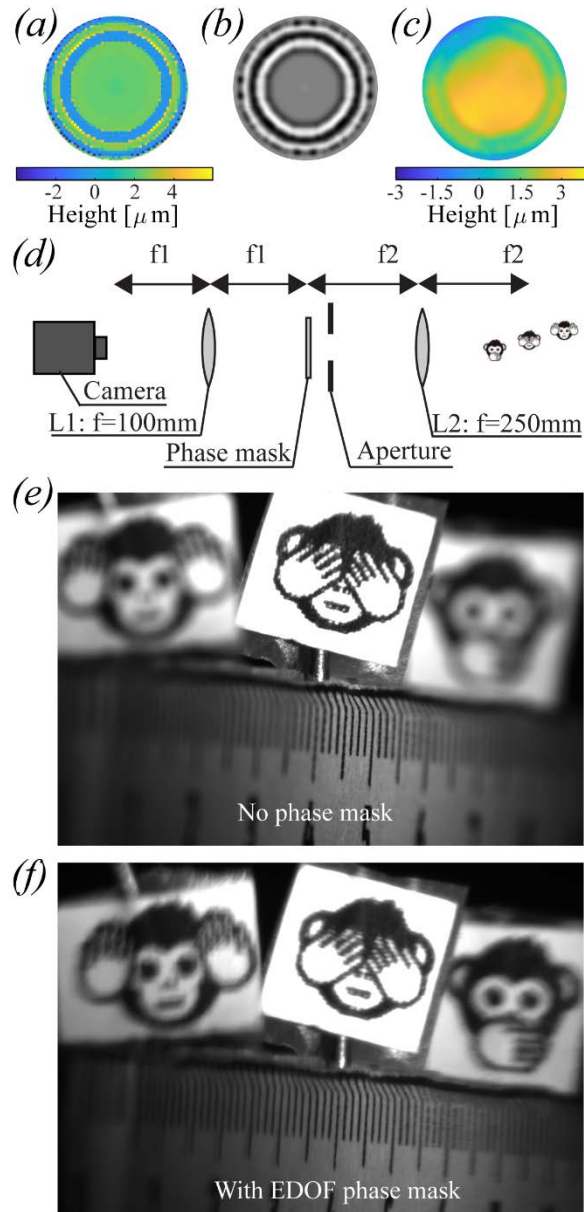


Figure 4 | Fabrication and demonstration of an extended depth of field phase mask. (a) The design of the extended depth of field (EDOF) mask based on Nehme et al. [30]. (b) The projection pattern for a negative mold, as solved by the inverse problem. (c) The obtained phase mask as measured by the DHM. (d) Schematic illustration of the optical setup. We position the phase mask in the Fourier plane of a $4f$ system, and image three targets positioned 2.5 cm from one other. We used an additional small fixed aperture to ensure that the phase mask itself does not reduce the aperture stop. (e) The resulting image without the phase mask, showing only the center target in focus. (j) The resulting image with the EDOF phase mask showing all three targets in focus.

Three-dimensional localization microscopy uses phase masks positioned in the Fourier plane of a microscope to modify the PSF in order to encode three-dimensional information [2]. Figure 5 presents the use of the inverse problem approach for fabrication of such a phase mask. Figure 5a

presents the topography of the desired ‘tetrapod’ mask [23], designed to provide depth information over a range of $\pm 2 \mu\text{m}$. Here, too, we use the desired mold topography as input to equation (3) and obtain the intensity map presented in Figure 5b. The parameters used in the solution are identical to those that were used in Figure 4 and that are detailed in SI section 3. Figure 5c presents the topography of the resulting phase mask created by casting PDMS onto the resulting mold, as measured by the DHM. The first column in Figure 5d presents the measured PSF of a single emitter (a 200 nm fluorescent bead) at different locations along the optical axis, in the absence of any phase mask. The second column presents the measured PSF of the same emitter, when using a phase mask produced using a 3-step lithography process. The last column in Figure 5d presents the measured PSF as obtained using our phase mask fabricated by the thermocapillary fluidic shaping method. Figure 5e demonstrates the use of this mask for 3D tracking of three 200 nm beads undergoing Brownian motion (see Supplementary Video 1) in a liquid environment, and of one stationary bead (attached to the bottom surface)

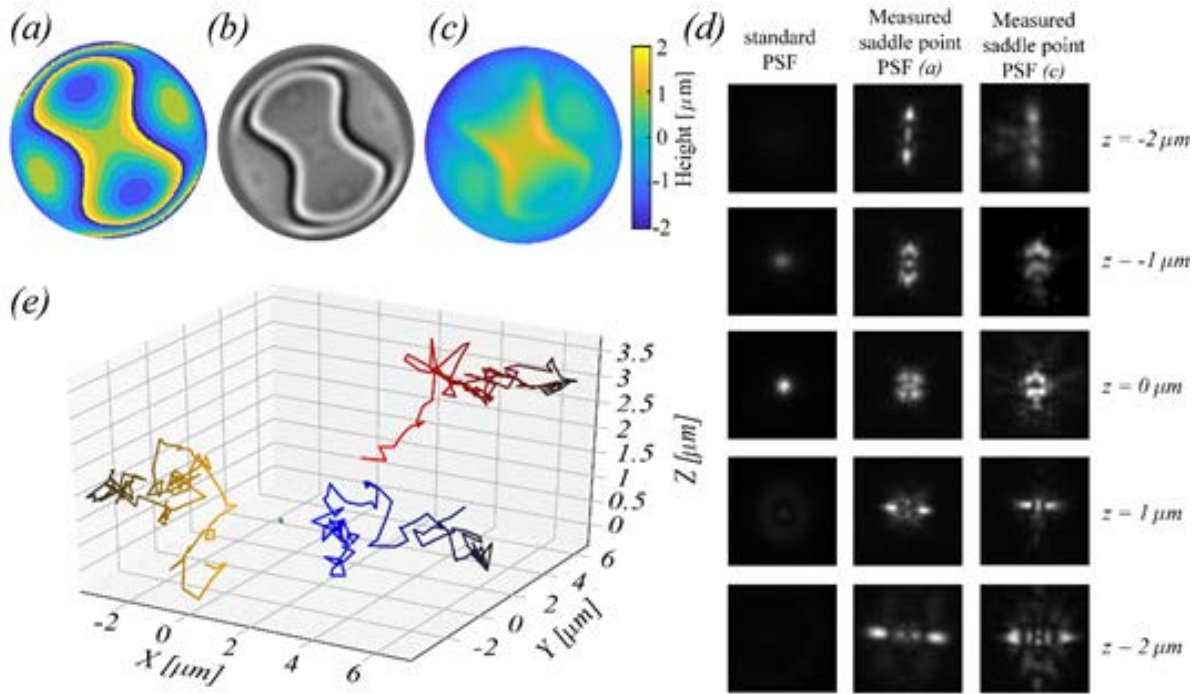


Figure 5 | Fabrication and demonstration of a saddle point phase mask for three-dimensional localization microscopy. (a) Topography map of a saddle point phase mask microfabricated using standard lithography and ion etching processes. (b) The illumination pattern required for deforming the liquid film into a negative mold for the phase mask, as obtained from the inverse problem solution. (c) DHM measurement of the resulting solidified PDMS mask, cast on the mold fabricated by thermocapillary fluidic shaping. (d) The PSF of a 200 nm diameter fluorescent microsphere at various z positions, as obtained from (i) a measured standard PSF with no phase mask (ii) a measured PSF using a lithography phase mask, (iii) a measured PSF using the mask obtained through thermocapillary fluidic shaping. (e) Tracking of three nanobeads undergoing Brownian motion and one stationary bead (in green) in a liquid, using the fabricated mask.

DISCUSSION

In this work, we introduced a novel method for rapid fabrication of diffractive optical elements via thermocapillary shaping of liquid polymer films. We provided a theoretical model for the inverse problem, making it possible to design specific topographies corresponding to desired optical functionalities. This approach has several significant advantages over existing fabrication technologies. First and foremost, the method is programmable in the sense that the desired deformation is created in response to the projected pattern. Thus, a single setup can be used to implement a wide range of different designs. Once the liquid element is exposed to UV light, it undergoes rapid solidification (in under 5 minutes) and results in a molecularly smooth solid element. The short fabrication time scale makes the method especially attractive for rapid prototyping of DOE's, allowing maximal flexibility for testing various optical designs. To illustrate the utility of the method, we fabricated several DOE's and demonstrated their functionality.

Using our current setup, we were able to achieve deformations on the order of several microns over a lateral span of millimeters. The magnitude of deformations is sufficient for most applications in the visible spectrum, as it allows for phase accumulation of at least 2π . However, achieving higher spatial resolution is certainly desirable in order to allow the production of more sophisticated DOEs. Higher resolution would be achieved if stronger temperature gradients could be generated on the film. The current resolution is limited by the natural heat convection from the liquid film, i.e. simply increasing the projection intensity would increase the temperature not only on the illuminated pixels but also in their surroundings, thus reducing the gradient. Therefore, to achieve higher resolutions, we must include effective heat removal strategies. This could be achieved, for example, by placing the entire setup at a lower ambient temperature, or by designing a heat exchanger at the bottom surface. Clearly, in order to maintain the flexibility of projection, such a heat exchanger must be sufficiently transparent to allow the projected light to reach the absorbing pads.

Our inverse problem solution provides the temperature distribution required for a desired deformation. In our implementation, we assume a linear relation between the desired temperature and the projected light intensity. However, this assumption must be verified, and may be the source of deviation between the desired and obtained topographies. More generally – an empirical model relating the temperature to projection intensity should ideally be created. To do so, the temperature on the liquid interface should be measured, requiring high resolution and high precision thermal imaging. Alternatively, the topography of the liquid film could be measured in real-time (e.g. by interferometry) allowing to close a loop and modify the projection pattern dynamically to match the desired shape before the element is solidified. Another attractive feature of this approach is the simplicity and affordability of the required setup, consisting of a simple projector and a reusable substrate containing an array of light-absorbing metal pads. As such, this technology can be easily scaled up and implemented in any laboratory, allowing for low-cost customized fabrication of DOEs for both research and industrial applications.

ACKNOWLEDGEMENTS

We thank Baruch Rofman for performing the AFM measurements for surface roughness characterization. This project has received funding from the European Research Council (ERC) under the European Union's Horizon 2020 Research and Innovation Programme, Grant Agreement No. 678734 (MetamorphChip).

AUTHOR CONTRIBUTIONS

V.F and M.B. conceived the method. R.E. developed the experimental setup, performed the thermocapillary experiments, collected and analyzed the data. V.F. and M.N. developed the theory. R.E., V.F., O.L., M.N., and M.B. designed the experiments. O.L. designed and simulated the light absorption layer. K.G. fabricated the devices. M.S. designed and built the digital mirror device module. Y.S. conceived the optical experiments. B.F. designed the phase masks. R.E., and N.O. designed and performed the 3D localization experiments. R.E. and M.B. wrote the manuscript. All authors reviewed and commented on the manuscript.

COMPETING INTERETS

The authors declare that they have no competing interests.

REFERENCES

- [1] M. Born and E. Wolf, *Principles of Optics: Electromagnetic Theory of Propagation, Interference and Diffraction of Light* (Elsevier, 2013).
- [2] S. R. P. Pavani, M. A. Thompson, J. S. Biteen, S. J. Lord, N. Liu, R. J. Twieg, R. Piestun, and W. E. Moerner, *Three-Dimensional, Single-Molecule Fluorescence Imaging beyond the Diffraction Limit by Using a Double-Helix Point Spread Function*, *Proceedings of the National Academy of Sciences* **106**, 2995 (2009).
- [3] D. Wildanger, J. Bückers, V. Westphal, S. W. Hell, and L. Kastrup, *A STED Microscope Aligned by Design*, *Opt. Express* **17**, 16100 (2009).
- [4] E. R. Dufresne and D. G. Grier, *Optical Tweezer Arrays and Optical Substrates Created with Diffractive Optics*, *Review of Scientific Instruments* **69**, 1974 (1998).
- [5] D. Xu, K. P. Chen, K. Ohlinger, and Y. Lin, *Holographic Fabrication of Diamondlike Photonic Crystal Template Using Two-Dimensional Diffractive Optical Elements*, *Appl. Phys. Lett.* **93**, 031101 (2008).
- [6] X. Lin, Y. Rivenson, N. T. Yardimci, M. Veli, Y. Luo, M. Jarrahi, and A. Ozcan, *All-Optical Machine Learning Using Diffractive Deep Neural Networks*, *Science* **361**, 1004 (2018).
- [7] L. Tan, J. Yu, J. Ma, Y. Yang, M. Li, Y. Jiang, J. Liu, and Q. Han, *Approach to Improve Beam Quality of Inter-Satellite Optical Communication System Based on Diffractive Optical Elements*, *Opt. Express* **17**, 6311 (2009).
- [8] I. Mingareev, R. Berlich, T. J. Eichelkraut, H. Herfurth, S. Heinemann, and M. C. Richardson, *Diffractive Optical Elements Utilized for Efficiency Enhancement of Photovoltaic Modules*, *Opt. Express* **19**, 11397 (2011).
- [9] R. Tyson, *Principles of Adaptive Optics*, 310 (n.d.).

- [10] D. C. O'Shea, T. J. Suleski, A. D. Kathman, and D. W. Prather, *Diffraction Optics* (SPIE, 1000 20th Street, Bellingham, WA 98227-0010 USA, 2003).
- [11] J. P. Rolland, M. A. Davies, T. J. Suleski, C. Evans, A. Bauer, J. C. Lambropoulos, and K. Falaggis, *Freeform Optics for Imaging*, *Optica* **8**, 161 (2021).
- [12] W. Kordonski, *MAGNETORHEOLOGICAL FLUIDS IN HIGH PRECISION FINISHING*, in *Electro-Rheological Fluids and Magneto-Rheological Suspensions* (WORLD SCIENTIFIC, Philadelphia, USA, 2011), pp. 30–39.
- [13] F. Kotz, A. S. Quick, P. Risch, T. Martin, T. Hoose, M. Thiel, D. Helmer, and B. E. Rapp, *Two-Photon Polymerization of Nanocomposites for the Fabrication of Transparent Fused Silica Glass Microstructures*, *Adv. Mater.* 2006341 (2021).
- [14] Ebstein, Steven M. "Nearly index-matched optics for aspherical, diffractive, and achromatic-phase diffractive elements." *Optics letters* 21.18 (1996): 1454-1456.
- [15] P. Berto, L. Philippet, J. Osmond, C. F. Liu, A. Afridi, M. Montagut Marques, B. Molero Agudo, G. Tessier, and R. Quidant, *Tunable and Free-Form Planar Optics*, *Nat. Photonics* **13**, 649 (2019).
- [16] Q. Wang, E. T. F. Rogers, B. Gholipour, C.-M. Wang, G. Yuan, J. Teng, and N. I. Zheludev, *Optically Reconfigurable Metasurfaces and Photonic Devices Based on Phase Change Materials*, *Nature Photon* **10**, 60 (2016).
- [17] C. V. Brown, G. G. Wells, M. I. Newton, and G. McHale, *Voltage-Programmable Liquid Optical Interface*, *Nature Photon* **3**, 403 (2009).
- [18] G. G. Wells, N. Sampara, E. E. Kriezis, J. Fyson, and C. V. Brown, *Diffraction Grating with Suppressed Zero Order Fabricated Using Dielectric Forces*, *Opt. Lett.* **36**, 4404 (2011).
- [19] Gabay, Israel, et al. "Shaping liquid films using dielectrophoresis." *arXiv preprint arXiv:2102.11019* (2021).
- [20] J. P. Singer, *Thermocapillary Approaches to the Deliberate Patterning of Polymers*, *Journal of Polymer Science Part B: Polymer Physics* **55**, 1649 (2017).
- [21] I. Nejati, M. Dietzel, and S. Hardt, *Exploiting Cellular Convection in a Thick Liquid Layer to Pattern a Thin Polymer Film*, *Applied Physics Letters* **108**, 051604 (2016).
- [22] E. McLeod, Y. Liu, and S. M. Troian, *Experimental Verification of the Formation Mechanism for Pillar Arrays in Nanofilms Subject to Large Thermal Gradients*, *Phys. Rev. Lett.* **106**, 175501 (2011).
- [23] Y. Shechtman, S. J. Sahl, A. S. Backer, and W. E. Moerner, *Optimal Point Spread Function Design for 3D Imaging*, *Phys. Rev. Lett.* **113**, 133902 (2014).
- [24] B. Ferdman, E. Nehme, L. E. Weiss, O. Alalouf, and Y. Shechtman, *VIPR: Vectorial Implementation of Phase Retrieval for Fast and Accurate Microscopic Pixel-Wise Pupil Estimation*, 20 (n.d.).
- [25] M. Tan, S. Bankoff, and S. H. Davis, *Steady Thermocapillary Flows of Thin Liquid Layers. I. Theory*, *Physics of Fluids A: Fluid Dynamics* **2**, 313 (1990).
- [26] E. Cuhe, P. Marquet, and C. Depeursinge, *Simultaneous Amplitude-Contrast and Quantitative Phase-Contrast Microscopy by Numerical Reconstruction of Fresnel off-Axis Holograms*, *Applied Optics* **38**, 6994 (1999).

- [27] Loewen, Erwin G., and Evgeny Popov. *Diffraction gratings and applications*. CRC Press, 2018.
- [28] E. R. Dowski and W. T. Cathey, *Extended Depth of Field through Wave-Front Coding*, *Appl. Opt.* **34**, 1859 (1995).
- [29] E. Ben-Eliezer, E. Marom, N. Konforti, and Z. Zalevsky, *Experimental Realization of an Imaging System with an Extended Depth of Field*, *Appl. Opt.* **44**, 2792 (2005).
- [30] E. Nehme, B. Ferdman, L. Weiss, T. Naor, D. Freedman, T. Michaeli, and Y. Shechtman, *Learning Optimal Wavefront Shaping for Multi-Channel Imaging*, *IEEE Trans. Pattern Anal. Mach. Intell.* **1** (2021).

METHODS

Thermocapillary shaping experimental setup

The experimental setup consists of a glass substrate patterned with metallic pads fabricated by liftoff photolithography processes. The pads consist of two metallic layers - a 150 nm chromium layer, followed by a 50 nm gold layer. The metal pads were then coated with a 400 nm silicon dioxide layer to protect them. We used PVC tape to form the boundaries of a 2 cm x 2 cm x 60 μm fluidic chamber on top of the patterned substrate. Before filling the fluidic chamber, we treated the device with low-pressure air plasma (Zepto W6, Diener Electronics, Germany) for 1 min, allowing for improved wetting of the substrate. Next, we injected ~15 μl of a UV curable polymer (CPS 1050 UV, Colorado Photopolymer Solutions, USA) to fill the chamber. We covered the chamber with a UV-transparent polystyrene lid to protect the polymer from contamination. The illumination system (depicted in figure 1) consists of a liquid guide connected to a computer-controlled LED light source (Sola SE, Lumencore, USA) and a beam expander composed of two lenses: L1, an aspherical condenser (ACL25416U-A, Thorlabs, USA) and L2, a biconvex lens (LB1723-A, Thorlabs, USA) to magnify the beam. We collimate the light into a digital mirror device (1024 x 768 pixels, V7001, Texas Instruments, USA), allowing the projection of any desired shape. The projected light passed through L3, a Kohler lens with $f=300$ mm (AC254-300-A, Thorlabs, USA), which focuses the light onto the back focal plane of the microscope objective (PlanApo, 10x, NA=0.45, Nikon, Japan). To create a desired deformation, we illuminate the bottom of the device with a corresponding light pattern and allow 1 minute for equilibration. We then position the UV lamp (24 W, $\lambda=370$ nm) at a distance of ~20 mm above the substrate and illuminate for 4 min to cure the polymer into a solid element. We measure the topography of the resulting components using a digital holographic microscope (DHMR1003, LynceeTec, Switzerland).

Fabrication of PDMS based DOEs

We fabricated our DOEs by casting Polydimethylsiloxane (PDMS) at a ratio of 1:10 (cross-linker to resin) on top of the solidified UV polymer, after treating the polymer surface with Chlorotrimethylsilane (Sigma Aldrich, Germany). After casting the PDMS, we placed the mold in a vacuum chamber for 3 hours for degassing, followed by 3 hours at 60⁰ C in the oven for curing.

Engineered point spread function measurement and bead tracking

We placed the PDMS phase mask in the Fourier plane of a $4f$ system, located on the imaging exit of an inverted microscope (Ti2, Nikon, Japan) equipped with a 100x objective (CFI SR HP Plan Apochromat Lambda S 100XC Si1, Nikon, Japan). To create the reference z-stack, we deposited 200 nm diameter fluorescent emitters (TetraSpeck, Thermo Fisher, USA) on a glass slide and excited them with a combination of a 488 nm and 532 nm lasers. We then imaged the point spread functions (PSFs) of the optical system containing the tetrapod phase mask, as a function of the z coordinate of the beads over an

axial range of 4.5 μm with steps of 50 nm. The z-stack was used to estimate the optical system's pupil function using phase retrieval [24].

We then placed the same type of beads in a water-glycerol mixture, allowed to move freely under Brownian motion, and imaged them using the tetrapod phase mask. We then used the z-stack to retrieve their three dimensional coordinates, using a maximum likelihood estimation, per frame.

Diffraction grating measurement

To measure the diffraction through the fabricated grating, we transmitted collimated monochromatic light through the grating and measured the diffraction pattern on a camera sensor (D90, Nikon, Japan) located at a distance of 1 m. We repeated this using three different LEDs sources (M660F1, M530F1, M470F1, Thorlabs, USA) with spectral peaks at 660 nm, 530 nm and 470 nm. The three LEDs were fiber coupled, allowing the use of a single collimation setup, and switching of the light sources by connecting the fiber input to the different sources. The collimation setup was based on an aspheric condenser (ACL25416U-A, Thorlabs, USA) focused onto a 50 μm pinhole, and 2x objective (Plan UW, NA 0.06, Nikon, Japan) for collection of the light.

EDOF measurement

The imaging setup is presented in figure 5d. The $4f$ imaging system consists of two lenses, L1 (AC254-100-A, Thorlabs, USA) and L2 (AC254-250-A, Thorlabs, USA), and a monochromatic CCD sensor. The phase mask was placed at the Fourier plane of the system, and an aperture was located adjacent to it. In the reference experiment, the phase mask was removed, but the aperture was maintained, to ensure the same aperture stop for both cases. The imaged target consisted of three of three ~ 5 mm printed figures connected to a ruler and located at distances of 247.5 mm, 250 mm, and 252.5 mm from the L2 lens.

Supplementary Material

Fabrication of diffractive optical elements by programmable thermocapillary shaping of thin liquid films

Ran Eshel¹, Valeri Frumkin^{1,§}, Matan Nice¹, Omer Luria¹, Boris Ferdman^{2,3}, Nadav Opatovski², Khaled Gommed¹, Maxim Shusteff⁴, Yoav Shechtman^{2,3}, and Moran Bercovici^{1,2,3,*}

¹ Faculty of Mechanical Engineering, Technion - Israel Institute of Technology, Haifa, 3200003 Israel

² Department of Biomedical Engineering, Technion - Israel Institute of Technology, Haifa, 3200003 Israel

³ Russell Berrie Nanotechnology Institute, Technion - Israel Institute of Technology, Haifa, 3200003 Israel

⁴ Lawrence Livermore National Laboratory, 7000 East Ave, Livermore, CA 94550, USA

[§] Current affiliation: Department of Mathematics, Massachusetts Institute of Technology, Cambridge, MA, 02139, United States

Table of Contents

S.1. Additional experimental data	2
Characterization	2
Surface roughness measurements	4
S.2. Solutions to the inverse problem	5
One dimensional analysis	5
Two-dimensional analysis	5
S.3. Numerical verification of the two-dimensional inverse problem solution	7
S.4. Material properties	9
Appendix A: Derivation of the steady-state equation for the shape of thin liquid film subjected to a non-uniform temperature distribution	10
Governing equations and boundary conditions in dimensional form	10
Scaling and asymptotics	11
Thermocapillary effect	13
References	14

S.1. Additional experimental data

Characterization

Figure S1 provides a characterization of the local deformation induced by the projection of an isolated circular spot, as a function of the projection intensity, and for several different geometric configurations of the metallic pads. In all cases, the system was allowed to achieve a steady state, at which point the polymer film was solidified and its surface was measured using a digital holographic microscope (DHM) [1]. Figure S1 presents a cross-section of the resulting axisymmetric film deformation, relative to an initial film thickness of $60\ \mu\text{m}$, as a function of the illumination intensity. Here, the diameter of the illumination spot is $500\ \mu\text{m}$, and the absorbing metal pad array consists of $20 \times 20\ \mu\text{m}$ pads with an edge-to-edge distance of $80\ \mu\text{m}$. As expected, the magnitude of the resulting deformation is proportional to the illumination intensity, and this correlation is linear with a maximum deformation of approximately $1.2\ \mu\text{m}$, as shown in the inset. The width of the deformation also increases with intensity, yet more moderately, from $\sim 0.6\ \text{mm}$ to $\sim 0.8\ \text{mm}$. Further increase in deformation magnitude can be achieved by increasing the pad array density. Figure S1b shows the resulting deformation as a function of the spacing between the absorbing metal array pads, for the same spot size at a fixed (maximum) projection intensity. The results show that a higher pad density leads to absorbance of a larger fraction of light, resulting in increased heating and larger deformation. The inset shows a linear correlation between the area fraction of the surface covered with metal pads and the deformation magnitude, reaching a maximum of approximately $3\ \mu\text{m}$. Interestingly, the width of the deformation over this range remains nearly constant. Figure S1c provides information on the repeatability of the resulting deformation by projecting the same spot size and intensity in three independent experiments using the maximum intensity of the light source. Figure S1d presents an isometric view and cross-sections of the resulting deformation for a $500\ \mu\text{m}$ spot size. As expected, for a circular spot, the resulting deformation is axisymmetric.

Figure S2 presents the deformation due to projection of an annulus pattern, with a linear increase in projection intensity along its azimuth, providing a characterization of the achievable deformation resolution. Figure S2a presents the solidified polymer topography as measured by the DHM. Figure S2b presents the projection intensity (blue line) and the resulting deformation magnitude (red circles), along the azimuthal coordinate along path indicated by the red dashed circle in Figure S2a. We find that the deformation correlates well with the light intensity, and the deformation is able to follow a discontinuity in the light intensity with a slope of $5.41\ \mu\text{m}/\text{mm}$. Figure S2c presents the cross sections of the deformation at the azimuthal coordinates indicated by corresponding gray lines in Figure S2a. The green squares in Figure S2b show the average over the full width at half maximum (FWHM) of these deformation profiles as a function of the azimuthal coordinate. The direct dependence of the width on the intensity is shown in Figure S3d.

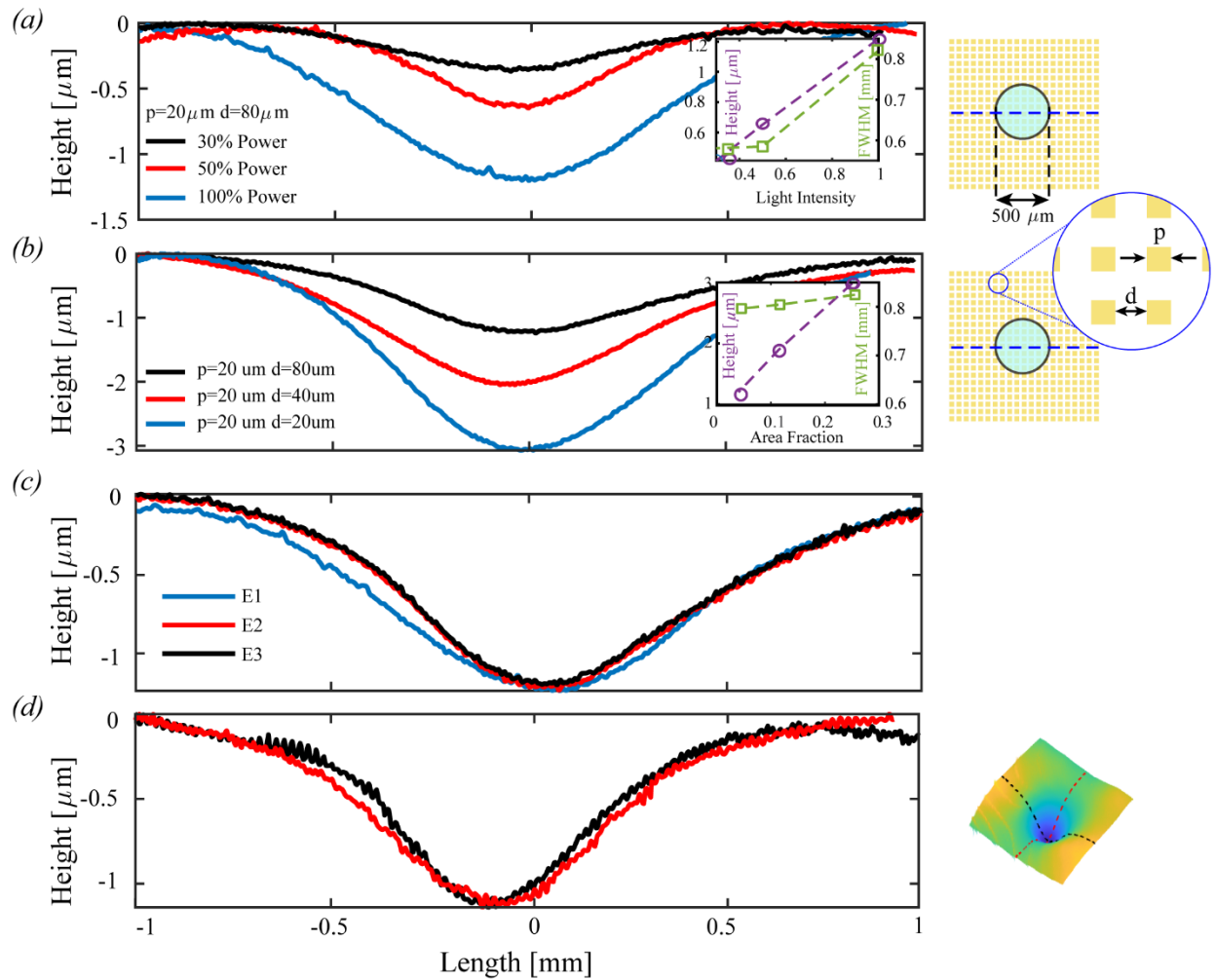


Figure S1 | Experimental characterization of the deformation magnitude and shape. (a) A cross-section of the deformation along the horizontal axis (as indicated by the dashed blue line) as a function of the illumination intensity, for a fixed pad geometry ($p = 20 \mu\text{m}$, $d = 80 \mu\text{m}$). As shown in the inset, the deformation magnitude increases linearly with the illumination intensity. The width of the deformation shows a moderate increase between 50% and 100% intensity. (b) A cross section of the deformation along the horizontal axis as a function of the edge-to-edge distance between pads ($d = 20, 40, 80 \mu\text{m}$), for a fixed illumination intensity (100%) and a fixed pad size ($p \times p = 20 \times 20 \mu\text{m}$). As the gap decreases, a larger fraction of the light per unit area is absorbed, allowing further increase in deformation magnitude. Under these conditions, the width of the deformation is essentially unaffected by the gap size. (c) A cross section of the deformation for three repeats at the same intensity. (d) A horizontal and vertical cross section of the deformation, showing good agreement. All the results in the figure were obtained using a $60 \mu\text{m}$ film thickness and a $500 \mu\text{m}$ diameter disk-shaped projection.

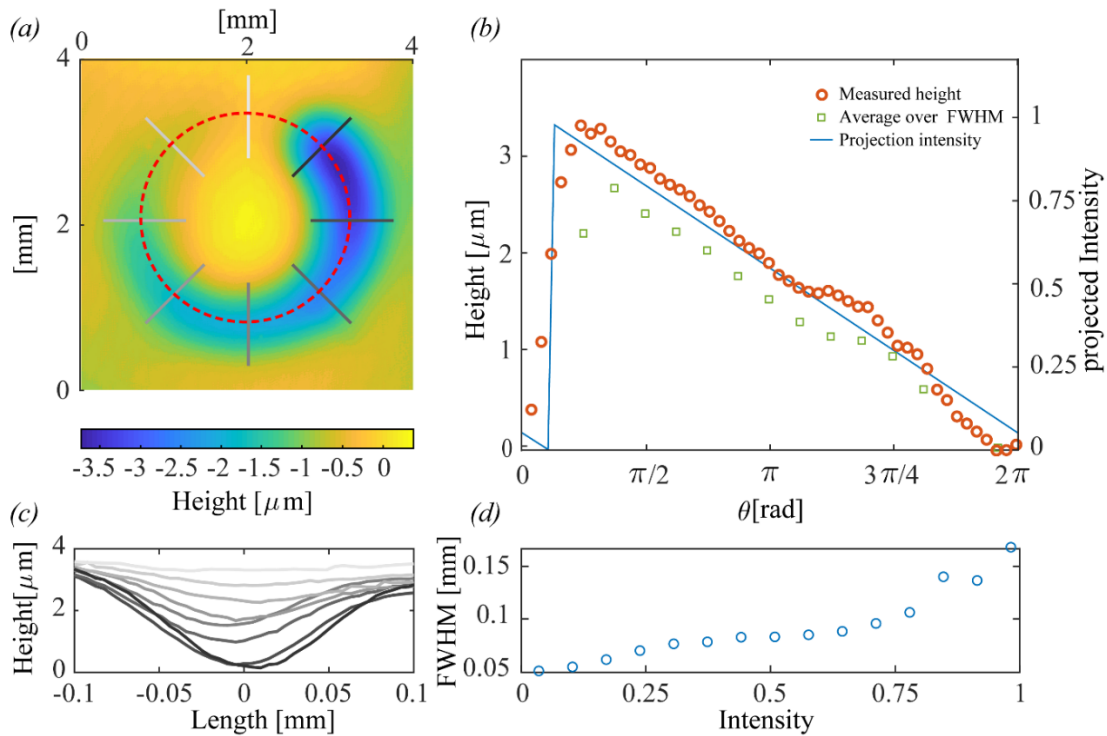


Figure S2 | Characterization of deformation resolution as a function of projection intensity. (a) Experimental result showing the spatial deformation resulting from projection of an annulus of width $200\ \mu\text{m}$ with an azimuthally varying intensity from 0 to 100%. (b) The magnitude of the deformation (red circles) and the width (FWHM, green squares) at each azimuthal coordinate, together with the projection intensity (blue line) along the centerline of the annulus (red dashed line in a). (c) Radial cross-sections of the deformation at different azimuthal locations as indicated by corresponding grayscale lines in a. (d) Full width at half maximum of the deformation as a function of intensity along the annulus pattern.

Surface roughness measurements

Figure S3 presents a representative atomic force microscopy (AFM) measurement that we performed over an area of $2.2 \times 2.2\ \mu\text{m}$ in order to evaluate the surface roughness of the solidified polymer surface. The resulting topography shows a surface roughness of less than 1 nm RMS over the measured area, which is excellent for nearly all optical applications.

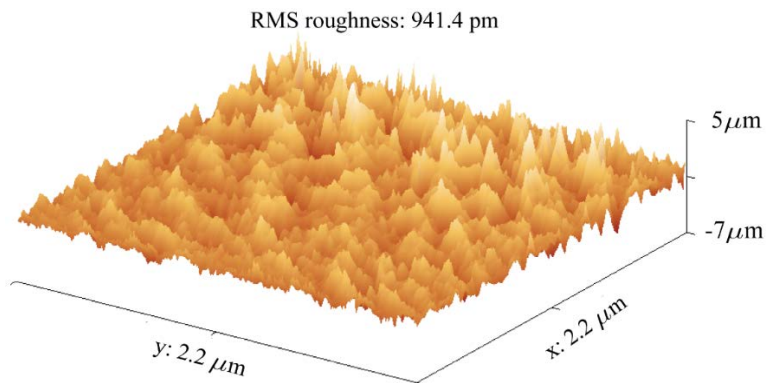


Figure S3 | AFM measurement of the surface of the solidified polymer. The RMS of the surface roughness is less than 1 nm.

S.2. Solutions to the inverse problem

We are interested in solving the inverse problem, namely, finding the temperature field required to create a desired deformation.

The differential equation describing the steady state deformation of a thin liquid film subjected to a non-uniform temperature gradient is given by (see Appendix A for detailed derivation)

$$\nabla \cdot \left[\frac{S}{3} H^3 \bar{\nabla} \nabla^2 H - \frac{G}{3} H^3 \bar{\nabla} H - \frac{1}{2} H^2 \bar{\nabla} \left(\frac{\vartheta_b + \Theta}{1 + BH} \right) \right] = 0, \quad (S1)$$

where H is the dimensionless distance of the free surface from the flat rigid floor, ϑ_b is the temperature distribution on the bottom surface, S is the inverse capillary number, G is the gravitation number, B is the Biot number, and Θ is the scaled magnitude of the temperature at infinity (see details in the Appendix).

One dimensional analysis

We start by obtaining a solution to the inverse problem for the one-dimensional case, described by

$$\partial_x \left[\frac{S}{3} H^3 \partial_x^3 H - \frac{G}{3} H^3 \partial_x H - \frac{1}{2} H^2 \partial_x \left(\frac{\vartheta_b + \Theta}{1 + BH} \right) \right] = 0, \quad (S2)$$

where X is the non-dimensional spatial coordinate. We assume that the temperature variations occur far from the boundaries, $X = \pm \mathcal{L}$, and therefore at the boundaries the film can be assumed to be flat.

$$H(\pm \mathcal{L}) = 1, \quad \partial_x^n H(\pm \mathcal{L}) = 0 \{n = 1, 2, 3\}, \quad \vartheta_b(\pm \mathcal{L}) = -\Theta, \quad \partial_x \vartheta_b(\pm \mathcal{L}) = 0. \quad (S3)$$

Integrating equation (S2) in X and dividing by H^2 we obtain

$$\frac{S}{3} H \partial_x^3 H - \frac{G}{3} H \partial_x H - \frac{1}{2} \partial_x \left(\frac{\vartheta_b + \Theta}{1 + BH} \right) = \frac{C_0}{H^2}, \quad (S4)$$

where C_0 is an integration constant. The *LHS* can be integrated by parts, and vanishes when using the boundary conditions (S3),

$$\int_{-\mathcal{L}}^{\mathcal{L}} \left[\frac{S}{3} H \partial_x^3 H - \frac{G}{3} H \partial_x H - \frac{1}{2} \partial_x \left(\frac{\vartheta_b + \Theta}{1 + BH} \right) \right] dX = 0 \quad (S5)$$

Since the integration of the *RHS* of (S4) is non-zero, the coefficient C_0 must vanish, $C_0 = 0$.

The 1D steady state equation (S4) can thus be simplified to

$$\frac{S}{3} H \partial_x^3 H - \frac{G}{3} H \partial_x H - \frac{1}{2} \partial_x \left(\frac{\vartheta_b + \Theta}{1 + BH} \right) = 0. \quad (S6)$$

Integrating equation (S6) to an arbitrary position ξ yields an explicit expression for the temperature variation, $\vartheta_b(\xi)$, required in order to create the desired deformation $H(\xi)$.

$$\vartheta_b(\xi) = \frac{1 + BH(\xi)}{3} \left[2SH(\xi) \partial_\xi^2 H(\xi) - S \left(\partial_\xi H(\xi) \right)^2 - G(H(\xi)^2 - 1) \right] - \Theta. \quad (S7)$$

Two-dimensional analysis

The two-dimensional case cannot be directly integrated. We therefore propose an ansatz based on the 1D solution,

$$\vartheta_b = \frac{1 + BH}{3} \left[2SH\nabla^2 H - S(\vec{\nabla}H)^2 - G(H^2 - 1) \right] - \Theta, \quad (S8)$$

or in dimensional form,

$$\theta_b - \theta_\infty = \frac{1 + \frac{\hbar}{k}h}{3\beta} \left[2\sigma_r h \nabla^2 h - \sigma_r (\vec{\nabla}h)^2 - \rho g (h^2 - h_0^2) \right]. \quad (S9)$$

To test the validity of the proposed ansatz, we reconstruct a differential equation that yields this solution (S8), and check to what extent it deviates from (S1). Equation (S8) can be recast as

$$\frac{1}{2} \left(\frac{\vartheta_b + \Theta}{1 + BH} \right) = \frac{1}{6} \left(2SH\nabla^2 H - S(\vec{\nabla}H)^2 - G(H^2 - 1) \right), \quad (S10)$$

and taking its gradient then yields

$$\frac{1}{2} \vec{\nabla} \left(\frac{\vartheta_b + \Theta}{1 + BH} \right) = \frac{1}{3} \left(SH\vec{\nabla}\nabla^2 H + S\vec{\nabla}H\nabla^2 H - \frac{1}{2} S\vec{\nabla}(\vec{\nabla}H)^2 - GH\vec{\nabla}H \right). \quad (S11)$$

To compare equation (S11) to (S1), we note that equation (S1) can be written as $\vec{\nabla} \cdot (H^2 \vec{F}) = 0$, which can be satisfied by

$$\vec{F} = \frac{S}{3} H\vec{\nabla}\nabla^2 H - \frac{G}{3} H\vec{\nabla}H - \frac{1}{2} \vec{\nabla} \left(\frac{\vartheta_b + \Theta}{1 + BH} \right) = 0, \quad (S12)$$

or

$$\frac{1}{2} \vec{\nabla} \left(\frac{\vartheta_b + \Theta}{1 + BH} \right) = \frac{S}{3} H\vec{\nabla}\nabla^2 H - \frac{G}{3} H\vec{\nabla}H. \quad (S13)$$

Subtracting (S11) from (S13), we are left only with the second and third terms on the RHS of (S11),

$$0 = \frac{S}{6} \left[\vec{\nabla}(\vec{\nabla}H)^2 - 2\vec{\nabla}H\nabla^2 H \right]. \quad (S14)$$

The RHS in (S14) can thus be regarded as the difference between the approximate (ansatz) solution and the exact solution (S1),

$$\vec{\epsilon} = \frac{S}{6} \left[\vec{\nabla}[(\partial_X H)^2 + (\partial_Y H)^2] - 2\vec{\nabla}H(\partial_X^2 H + \partial_Y^2 H) \right], \quad (S15)$$

which can be written explicitly in terms of its components as

$$\vec{\epsilon} = \frac{S}{3} \left[(\partial_Y H \partial_{XY}^2 H - \partial_X H \partial_Y^2 H), (\partial_X H \partial_{XY}^2 H - \partial_Y H \partial_X^2 H) \right] \quad (S16)$$

The ansatz solution is thus exact when the non-normalized Gaussian curvature of the surface, $K = \partial_X^2 H \partial_Y^2 H - (\partial_{XY}^2 H)^2$, vanishes. For other surfaces, the error would depend on the magnitude of the Gaussian curvature, and we provide a numerical assessment for this error in the following section.

S.3. Numerical verification of the two-dimensional inverse problem solution

We seek a solution that will satisfy equation (S12),

$$F_x = \frac{S}{3}H\partial_x\nabla^2H - \frac{G}{3}H\partial_xH - \frac{1}{2}\partial_x\left(\frac{\vartheta_b + \Theta}{1 + BH}\right) = 0, \quad (\text{S17. } a)$$

$$F_y = \frac{S}{3}H\partial_y\nabla^2H - \frac{G}{3}H\partial_yH - \frac{1}{2}\partial_y\left(\frac{\vartheta_b + \Theta}{1 + BH}\right) = 0. \quad (\text{S17. } b)$$

By defining $T = \frac{\vartheta_b + \Theta}{1 + BH}$, the equations can be expressed as

$$\partial_x T = \frac{2}{3}H[S\partial_x(\nabla^2H) - G\partial_xH], \quad (\text{S18. } a)$$

$$\partial_y T = \frac{2}{3}H[S\partial_y(\nabla^2H) - G\partial_yH]. \quad (\text{S18. } b)$$

We specify a desired deformation map $H(X, Y)$ and integrate equation (S18.a) numerically in X from 0 to an arbitrary coordinate within the domain, ξ . The solution can be thus expressed as

$$T = A_1(\xi, Y) + A_2(Y), \quad (\text{S19})$$

where $A_1 = \int_{-\mathcal{L}}^{\xi} \frac{2}{3}H[S\partial_x(\nabla^2H) - G\partial_xH]dX$ is the result of the numerical integration and $A_2(Y)$ is an unknown function. Substituting (S19) into equation (S18.b) yields an equation for A_2 ,

$$\frac{d}{dY}A_2(Y) = \frac{2}{3}H[S\partial_y(\nabla^2H) - G\partial_yH] - \partial_y A_1(X, Y), \quad (\text{S20})$$

which we integrate numerically in Y between $-\mathcal{L}$ and an arbitrary coordinate within the domain, η , to find A_2 . The temperature field is then given by

$$\vartheta_b = (1 + BH)(A_1 + A_2) - \Theta \quad (\text{S21})$$

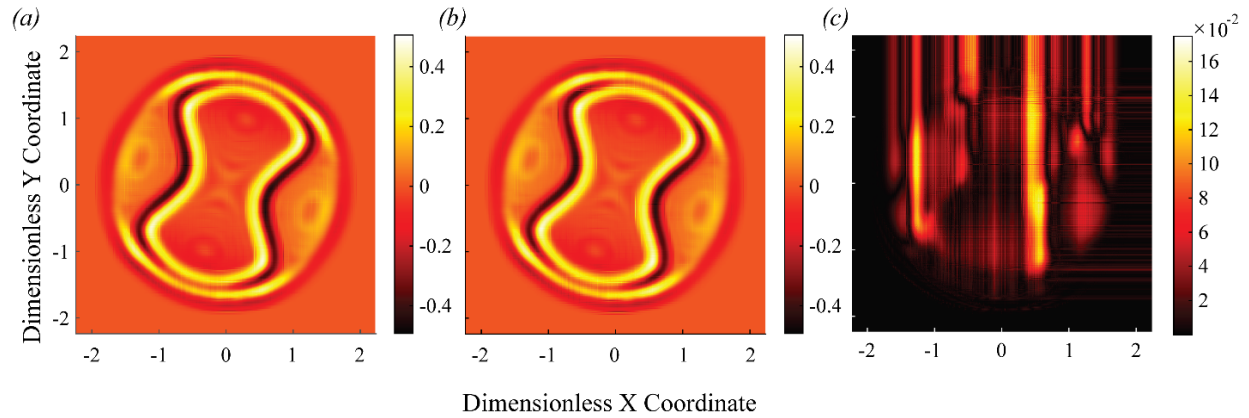


Figure S4 | A comparison between analytical and numerical solutions to the inverse problem of a tetrapod phase mask. (a) The dimensionless temperature based on the analytical solution S8. (b) The dimensionless temperature based the numerical solution S21. (c) The relative difference (in percent) between the analytical and numerical solutions, showing that the deviation is less than 0.17 %.

Figure S4 shows a comparison between the resulting dimensionless temperature obtained from the analytical solution (Figure S4a, corresponding to eq. S8) and from the numerical solution (Figure S4b, corresponding to eq. S21) for the case of the 3D localization microscopy mask ('tetrapod mask') presented

in Figure 5 of the main manuscript. For clarity of presentation, we subtracted from both solutions the mean temperature of the boundaries, so that the dimensionless temperature outside the mask area is set to zero. We defined the relative difference between the solutions as the absolute difference between them divided by the amplitude of temperature, and present the results in Figure S5c. As can be seen, the maximal relative difference is approximately 0.17 %.

S.4. Material properties

Table S1. Material properties that were used in all of the analytical and numerical solutions.

Property	Value	Units	Source
L_x, L_y	$6 \cdot 10^{-3}$	m	Chamber size
h_0	$60 \cdot 10^{-6}$	m	Calculated film thickness based on chamber size and injected volume
σ_r	28.5	$\frac{mN}{m}$	Based on the properties of the polymer CPS1050
β	0.866	$\frac{mN}{mK}$	Based on the properties of the polymer CPS1050
ρ	1200	$\frac{kg}{m^3}$	Based on the properties of NOA63
μ	2	$Pa \cdot s$	Based on the properties of NOA63
C_p	1632.852	$\frac{J}{kgK}$	Based on the properties of PSF-5cSt oil
k	$117.152 \cdot 10^{-3}$	$\frac{W}{mK}$	Based on the properties of PSF-5cSt oil
g	9.81	$\frac{m}{s^2}$	Earth's gravity acceleration
h	10	$\frac{W}{m^2K}$	Estimation based on common natural convection coefficients
$\theta_{b_{min}}, \theta_{b_{max}}$	23, 25	$^{\circ}C$	Assumed. Used for scaling only.
$\overline{\theta_b}$	24	$^{\circ}C$	Assumed. Used for scaling only.
θ_{∞}	23	$^{\circ}C$	Assumed. Used for scaling only.
l	$2 \cdot 10^{-3}$	m	Assumed. Used for scaling only.
$\nu = \frac{\mu}{\rho}$	$1.7 \cdot 10^{-3}$	$\frac{m^2}{s}$	Calculated
$\alpha = \frac{k}{\rho C_p}$	$5.979 \cdot 10^{-8}$	$\frac{m^2}{s}$	Calculated
$\Delta\theta = \theta_{b_{max}} - \theta_{b_{min}}$	2	$^{\circ}C$	Calculated

Appendix A: Derivation of the steady-state equation for the shape of a thin liquid film subjected to a non-uniform temperature distribution

We follow the derivation first presented by Vanhook et. al [2] and derive a 2D steady state equation for the free surface of a liquid film under the action of the thermocapillary effect. As illustrated in Figure S6, we consider a liquid with density ρ , dynamic viscosity μ , surface tension σ , thermal conductivity k , and heat capacity C_p , filling a shallow square-shaped cavity of length L , to an initial height h_0 .

A small subarea of the substrate with a characteristic length l is heated with a prescribed temperature $\theta_b(x, y)$, which is conducted to the free surface, yielding a non-uniform surface temperature. This yields surface tension gradients, which in turn lead to the transfer of mass along the interface, known as the thermocapillary effect [3]. Throughout the analysis we assume that the film thickness h_0 is significantly smaller than the characteristic length l , so that $\varepsilon = \frac{h_0}{l} \ll 1$.

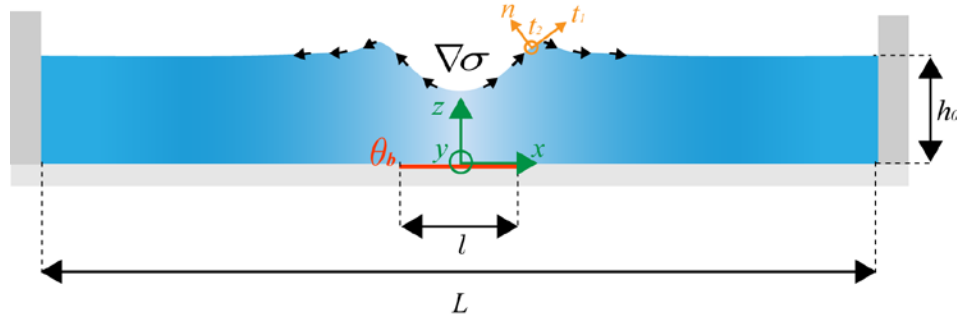


Figure S6 | Schematic description of the problem under consideration. A thin liquid film with an initial height h_0 , rests in a shallow, square-shaped cavity with a side length L . A small subarea of the substrate with a characteristic length l is heated with a prescribed temperature $\theta_b(x, y)$. The resulting non-uniform temperature distribution at the free surface induces gradients in surface tension, which, through the thermocapillary effect, lead to deformations of the liquid film.

Governing equations and boundary conditions in dimensional form

We separate our problem into a hydrodynamic problem and a thermal one, and begin with the prior. The governing equations are the continuity equation and steady-state Navier-Stokes (NS) equations,

$$\rho(\nabla \cdot \mathbf{U}) = 0, \quad (\text{A1. } a)$$

$$\rho \mathbf{U} \cdot \nabla \mathbf{U} = -\nabla p + \mu \nabla^2 \mathbf{U} + \rho \mathbf{g}, \quad (\text{A1. } b)$$

where \mathbf{U} is the three-dimensional velocity field, $\mathbf{g} = (0, 0, -g)$ is the gravity acceleration vector, and p is the pressure.

At $z = 0$ the liquid is subject to no-slip and no-penetration conditions,

$$\mathbf{U}(z = 0) = 0. \quad (\text{A2})$$

At the liquid-air interface, $z = h(x, y)$, the normal component of the velocity satisfies the kinematic boundary condition

$$w = \mathbf{u}_2 \cdot \nabla h, \quad (\text{A3. } a)$$

where $h = h(x, y)$ is the position of the free surface, $\mathbf{u}_2 = (u, v)$ is the planar velocity vector, $\nabla = (\partial_x, \partial_y)$ is the 2D gradient in the x and y directions, and w is the velocity component in the z direction.

Another boundary condition is a stress balance at the free surface,

$$(\bar{\mathbf{T}} - \bar{\mathbf{T}}_{air}) \cdot \mathbf{n} = 2\mathcal{H}\sigma\mathbf{n} + \partial_{t_1}\sigma \cdot \mathbf{t}_1 + \partial_{t_2}\sigma \cdot \mathbf{t}_2. \quad (\text{A3. b})$$

Here ∂_{t_i} is the directional derivative in the t_i direction ($i = 1,2$), $\bar{\mathbf{T}}$ and $\bar{\mathbf{T}}_{air}$ are the stress tensors in the liquid and air, respectively, \mathbf{n} and \mathbf{t}_i are the normal and tangential unit vectors, and $2\mathcal{H}$ is the mean curvature.

Scaling and asymptotics

We assume that the velocities in the x, y directions are of similar magnitude, and introduce the following scaling

$$\begin{aligned} U &= \frac{u}{U_0}, V = \frac{v}{U_0}, W = \frac{w}{W_0}, X = \frac{x}{l}, Y = \frac{y}{l}, Z = \frac{z}{h_0}, \\ H &= \frac{h}{h_0}, P = \frac{p}{P_0}, G = \frac{\rho h_0}{P_0}g, \Sigma = \frac{\sigma}{\Delta\sigma}, \end{aligned} \quad (\text{A4})$$

where $\Delta\sigma$ is a characteristic change in the surface tension resulting from temperature gradients, $\Delta\sigma = \beta\Delta\theta$. The dimensionless governing equations are hence:

$$\varepsilon U_0 \partial_X U + \varepsilon U_0 \partial_Y V + W_0 \partial_Z W = 0, \quad (\text{A5. a})$$

$$\varepsilon \text{Re} \left(U \partial_X U + V \partial_Y U + \frac{W_0}{U_0 \varepsilon} W \partial_Z U \right) = -\varepsilon \frac{h_0 P_0}{U_0 \mu} \partial_X P + (\varepsilon^2 \partial_X^2 U + \varepsilon^2 \partial_Y^2 U + \partial_Z^2 U),$$

$$\varepsilon \text{Re} \left(U \partial_X V + V \partial_Y V + \frac{W_0}{U_0 \varepsilon} W \partial_Z V \right) = -\varepsilon \frac{h_0 P_0}{U_0 \mu} \partial_Y P + (\varepsilon^2 \partial_X^2 V + \varepsilon^2 \partial_Y^2 V + \partial_Z^2 V), \quad (\text{A5. b})$$

$$\varepsilon \text{Re} \frac{W_0}{U_0} \left(U \partial_X W + V \partial_Y W + \frac{W_0}{U_0 \varepsilon} W \partial_Z W \right) = -\frac{h_0 P_0}{U_0 \mu} \partial_Z P + \frac{W_0}{U_0} (\varepsilon^2 \partial_X^2 W + \varepsilon^2 \partial_Y^2 W + \partial_Z^2 W) - \frac{h_0 P_0}{U_0 \mu} G,$$

where $\text{Re} = \frac{\rho U_0 h_0}{\mu}$ is the Reynolds number and U_0 will be defined in the following section. From the continuity equation (A5.a) we obtain the proper scaling for the velocity in the z direction, $W_0 = \varepsilon U_0$ and from the momentum equations (A5.b) we obtain the proper scaling for the pressure, $P_0 = \frac{\mu U_0}{\varepsilon h_0}$.

Projecting boundary condition (A3.b) onto the first tangential vector \mathbf{t}_1 yields the equation

$$\varepsilon P_0 (\partial_Y H \partial_Z U - \partial_X H \partial_Z V) = \frac{\Delta\sigma}{l} (\partial_X \Sigma \partial_Y H - \partial_Y \Sigma \partial_X H). \quad (\text{A6})$$

A similar result is achieved by projecting (A3.b) onto the second tangential vector, \mathbf{t}_2 . We substitute the definition of P_0 and rewrite (A6) as

$$\partial_Y H \left(\partial_Z U - \frac{\varepsilon \Delta\sigma}{\mu U_0} \partial_X \Sigma \right) - \partial_X H \left(\partial_Z V - \frac{\varepsilon \Delta\sigma}{\mu U_0} \partial_Y \Sigma \right) = 0. \quad (\text{A7})$$

Since we require the balance in (A7) to hold independently of the derivatives of H , we obtain the proper scaling for the velocity, $U_0 = \varepsilon \Delta\sigma / \mu$ and the dimensionless boundary conditions (A11.c).

In the normal direction, equation (A3.b) balances the external pressure with the surface tension. We assume that the overall change in surface tension, $\Delta\sigma$, is small relative to a reference surface tension σ_r ,

and will further discuss this in the thermal section. Considering the aforementioned assumption, we can write the surface tension as $\sigma \approx \sigma_r$ and by projecting boundary condition (A3.b) onto the normal vector \mathbf{n} , the normal stress balance condition in dimensionless form can be expressed as

$$-P_0 P = \frac{\varepsilon \sigma_r}{l} (\partial_X^2 H + \partial_Y^2 H). \quad (\text{A8})$$

Substituting the expression for P_0 we can rewrite equation (A8) as

$$-P = S (\partial_X^2 H + \partial_Y^2 H), \quad (\text{A9})$$

where $S = \varepsilon^3 \frac{\sigma_r}{\mu U_0} = \varepsilon^2 \frac{\sigma_r}{\Delta \sigma}$ is the surface tension number. For our case $\frac{\sigma_r}{\Delta \sigma} = 10^2 \sim 10^3$ and $\varepsilon^2 = O(10^{-3})$ therefore $S = O(1)$ and the balance is maintained.

With the obtained scaling, we now turn to asymptotic analysis of the NS equations (A5.b). Noting that for the typical values in our system $Re \ll 1$, the leading order of the equations take the form

$$\partial_Z^2 U = \partial_X P, \quad \partial_Z^2 V = \partial_Y P, \quad (\text{A10. a})$$

$$\partial_Z P = -G, \quad (\text{A10. b})$$

with the boundary conditions at $Z = 0$:

$$U = V = W = 0 \quad (\text{A11})$$

and at $Z = H$:

$$W = U \partial_X H + V \partial_Y H, \quad (\text{A12. a})$$

$$\partial_Z U = \partial_X \Sigma, \quad \partial_Z V = \partial_Y \Sigma, \quad (\text{A12. b})$$

$$-P = S [\partial_X^2 H + \partial_Y^2 H]. \quad (\text{A12. c})$$

Integrating the continuity equation (A5.a) in the Z direction, applying Leibniz's rule and using the boundary conditions (A11) and (A12.a) we obtain an integral form of the kinematic condition

$$\partial_X \int_0^H U dZ + \partial_Y \int_0^H V dZ = 0. \quad (\text{A13})$$

Solving for the velocity field as a function of the pressure gradient (equations (A10.a) with B.C.s (A11) and (A12.b)), plugging it into equation (A13), and performing the integration yields

$$\left[\partial_X \left(-\frac{\partial_X P H^3}{3} + \frac{\partial_X \Sigma H^2}{2} \right) + \partial_Y \left(-\frac{\partial_Y P H^3}{3} + \frac{\partial_Y \Sigma H^2}{2} \right) \right]_{Z=H} = 0. \quad (\text{A14})$$

Equation (A14) can be compactly written as

$$\nabla \cdot \left[\frac{H^2}{2} \vec{\nabla} \Sigma - \frac{H^3}{3} \vec{\nabla} P \right] = 0, \quad (\text{A15})$$

where $\vec{\nabla} = (\partial_X, \partial_Y)$.

Integrating equation (A10.b) with B.C. (A12.c) allows us to express the pressure gradient in terms of the dimensionless free surface,

$$\vec{\nabla}P = G\vec{\nabla}H - S\vec{\nabla} \cdot \nabla^2 H. \quad (A16)$$

Substituting (A16) into (A15) results in the final form of the equation for the steady-state position of the free surface,

$$\nabla \cdot \left[\frac{H^2}{2} \vec{\nabla}\Sigma - \frac{H^3}{3} (G\vec{\nabla}H - S\vec{\nabla} \cdot \nabla^2 H) \right] = 0. \quad (A17)$$

Thermocapillary effect

In order to evaluate $\vec{\nabla}\Sigma$ we proceed to solve the coupled thermal problem, which is governed by the steady state energy equation,

$$\mathbf{U} \cdot \vec{\nabla}\theta = \alpha(\partial_x^2\theta + \partial_y^2\theta + \partial_z^2\theta), \quad (A18)$$

where θ is the liquid's temperature and $\alpha = \frac{k}{\rho c_p}$ is its thermal diffusivity.

At $z = 0$ the liquid is subject to a prescribed temperature profile $\theta_b(x, y)$:

$$\theta(z = 0) = \theta_b(x, y), \quad (A19)$$

and the heat transfer at the liquid-air interface, $z = h(x, y)$, is described by Newton's cooling law:

$$k\vec{\nabla}\theta_h \cdot \mathbf{n} + \hbar(\theta_h - \theta_\infty) = 0, \quad (A20)$$

where \hbar is the heat transfer coefficient and θ_∞ is the ambient gas temperature.

We scale the temperature by $\vartheta = \frac{\theta - \bar{\theta}_b}{\Delta\theta}$, where $\Delta\theta = \theta_{b_{max}} - \theta_{b_{min}}$, and $\bar{\theta}_b$, $\theta_{b_{max}}$, $\theta_{b_{min}}$ are the average temperature at the base, and its maximum and minimum values, respectively.

Equation (A18) in dimensionless form is thus

$$\varepsilon \text{Pe}(U\partial_x\vartheta + V\partial_y\vartheta + W\partial_z\vartheta) = \varepsilon^2\partial_x^2\vartheta + \varepsilon^2\partial_y^2\vartheta + \partial_z^2\vartheta, \quad (A21)$$

where $\text{Pe} = \frac{U_0 h_0}{\alpha}$ is the thermal Peclet number. We note that in our case $\text{Pe} = \frac{\varepsilon \Delta\sigma h_0}{\alpha \mu} = O(10^{-3}) \ll 1$.

We proceed to write ϑ as an asymptotic expansion in ε , which at the leading order yields

$$\partial_z^2\vartheta = 0, \quad (A22)$$

with the boundary conditions

$$\begin{aligned} Z = 0: & \quad \vartheta_b = \frac{\theta_b - \bar{\theta}_b}{\Delta\theta}, \\ Z = H(X, Y): & \quad [\partial_z\vartheta + B(\vartheta + \Theta)]_{Z=H} = 0, \end{aligned} \quad (A23)$$

where ϑ_b is the dimensionless temperature distributions at the bottom surface, $\Theta = \frac{\bar{\theta}_b - \theta_\infty}{\Delta\theta}$ is a ratio between temperature differences, and $B = \frac{\hbar h_0}{k}$ is the Biot number.

Equation (A22) with B.C.s (A23) yields the temperature distribution inside the liquid film

$$\vartheta = \vartheta_b - \frac{(\vartheta_b + \Theta)B}{1 + BH} Z, \quad (\text{A24})$$

and hence $\vartheta|_{z=H} = \frac{\vartheta_b - BH\Theta}{1 + BH}$.

We assume that the surface depends solely on the temperature at the interface $\sigma = \sigma(\theta(x, y, z = h))$, and that for small variations in temperature the surface tension changes linearly such that

$$\Delta\sigma = -\beta\Delta\theta_{z=h}, \quad (\text{A25})$$

where β is a positive constant and a property of the material and $\Delta\theta_{z=h}$ is the variation in temperature at the interface. The negative sign on the RHS of (A25) represents a decrease in surface tension as the temperature increases. This is consistent with our previous assumption of small variations in surface tension since for the liquid we used $\frac{\beta}{\sigma_r} \approx 10^{-3} \frac{1}{^\circ\text{K}}$ and for our system $\Delta\theta_h \approx 1^\circ\text{K}$.

Using the chain rule, its gradient can be written as:

$$\vec{\nabla}\sigma = \frac{d\sigma}{d\theta} (\vec{\nabla}\theta_{z=h} + \Delta\theta\partial_z\theta_{z=h}\vec{\nabla}h). \quad (\text{A26})$$

In dimensionless form the surface tension gradient is

$$\vec{\nabla}\Sigma = -(\vec{\nabla}\vartheta_{z=H} + \partial_z\vartheta_{z=H}\vec{\nabla}H), \quad (\text{A27})$$

Substituting equation (A24) into (A27) we obtain

$$\vec{\nabla}\Sigma = -\vec{\nabla}\left(\frac{\vartheta_b + \Theta}{1 + BH}\right). \quad (\text{A28})$$

Further substituting equation (A28) into equation (A17) yields the final equation defining the relation between the prescribed temperature and the resulting surface topography:

$$\nabla \cdot \left[\frac{S}{3} H^3 \vec{\nabla} \nabla^2 H - \frac{G}{3} H^3 \vec{\nabla} H - \frac{1}{2} H^2 \vec{\nabla} \left(\frac{\vartheta_b + \Theta}{1 + BH} \right) \right] = 0. \quad (\text{A29})$$

References

- [1] E. Cuche, P. Marquet, and C. Depeursinge, Simultaneous Amplitude-Contrast and Quantitative Phase-Contrast Microscopy by Numerical Reconstruction of Fresnel off-Axis Holograms, *Applied Optics* **38**, 6994 (1999).
- [2] S. J. Vanhook, M. F. Schatz, J. B. Swift, W. D. McCormick, and H. L. Swinney, Long-Wavelength Surface-Tension-Driven Bénard Convection: Experiment and Theory, *J. Fluid Mech.* **345**, 45 (1997).
- [3] M. Tan, S. Bankoff, and S. H. Davis, Steady Thermocapillary Flows of Thin Liquid Layers. I. Theory, *Physics of Fluids A: Fluid Dynamics* **2**, 313 (1990).